Research Square

Preprints are preliminary reports that have not undergone peer review.
They should not be considered conclusive, used to inform clinical practice,
or referenced by the media as validated information.

Subdural vein-based segmentation model for localization of spinal dural arteriovenous fistula using contrast-enhanced MR angiography

Yupeng Zhang
Beijing Tian Tan Hospital
Wenhao Xia
Beijing Tian Tan Hospital
Xiaochen Wang
Beijing Tian Tan Hospital
Long Wang
Beijing Tian Tan Hospital
Bo Han
Beijing Tian Tan Hospital
Xiaodi Han
Beijing Tian Tan Hospital
Dapeng Mo
Beijing Tian Tan Hospital
Shengjun Sun
Beijing Tian Tan Hospital
Yongzhi Wang
Beijing Tian Tan Hospital
Wenqing Jia
coffeemd@163.com

Beijing Tian Tan Hospital

Article

Keywords:

Posted Date: June 28th, 2026

DOI: https://doi.org/10.21203/rs.3.rs-9984374/v1

License: This work is licensed under a Creative Commons Attribution 4.0 International License.
Read Full License

Additional Declarations: No competing interests reported.

Abstract

Traditional artery-based level localization of SDAVF with DSA is invasive, time-consuming, radiation-exposed, and susceptible to false-negative results. We developed RadicularSEUNet to facilitate this task by reconstruction of the junction point between spinal dura mater and intradural vein on contrast-enhanced MR angiography. This model was trained (n = 1600), validated (n = 200) and tested (n = 200) on synthetic SDAVF cases, then further evaluated on a retrospective cohort of 31 real CEMRA cases including SDAVF and other vascular malformation types. In the independent test set, RadicularSEUNet achieved high segmentation performance of intradural veinous network on synthetic data, with median Dice, centerline Dice coefficient (clDice), F0.5, and composite score values of 0.986, 0.986, 0.992, and 0.988, respectively. In the clinical cohort, the combined workflow correctly differentiated SDAVF from other malformation types and achieved 100% accuracy for level localization. RadicularSEUNet enables a novel vein-based, noninvasive and anatomical intuitive strategy for SDAVF level localization.

Introduction

Spinal dural arteriovenous fistula (SDAVF) is the most common type of spinal vascular malformation, accounting for approximately 70% of all spinal vascular malformations. It most frequently occurs in elderly men, and the thoracolumbar region is the most involved site [1]. Spinal digital subtraction angiography (DSA) remains the gold standard for confirming the diagnosis of SDAVF and localizing the segmental feeding artery. However, in clinical practice, a substantial proportion of cases may be angiographically negative or inconclusive, requiring repeated angiography or surgical exploration for definitive diagnosis. This is largely because spinal angiography is a technically demanding procedure. With increasing patient age, factors such as atherosclerosis of the thoracoabdominal aorta, vascular tortuosity, and stenosis of radicular artery orifices may prolong the procedure, increase radiation exposure, and reduce patient tolerance, thereby contributing to a high rate of missed diagnosis. Because delayed diagnosis is a major predictor of unfavorable functional recovery [2,3], there is an urgent need to develop a definitive, convenient, and noninvasive diagnostic tool for SDAVF.

To address this clinical need, contrast-enhanced MR angiography (CEMRA) has been increasingly used as a preliminary diagnostic tool for detecting and localizing SDAVF [4]. The most recent and advanced imaging technique in this context is time-resolved CEMRA. In a recent meta-analysis, the level of SDAVF was correctly predicted in 76% of cases [5]. These findings indicate that CEMRA is a promising localization tool but remains insufficient. Fistulous vessels within the dural sleeve are generally under 0.5 mm in diameter and cannot be reliably resolved with the current spatial resolution of CEMRA. Instead, it usually appears as a focal vascular cluster. During threshold-based postprocessing, this vascular structure is difficult to distinguish from the epidural venous plexus or noises and may be erroneously removed. Therefore, postprocessed CEMRA images of SDAVF rarely demonstrate the complete angioarchitecture, including the feeding artery, fistulous zone, radicular vein, and dilated perimedullary

veins. As a result, clinicians cannot interpret CEMRA in the same manner as DSA, in which diagnosis and localization are guided by the arterial flow direction.

In contrast, the radicular vein has a substantially larger diameter than the fistulous arterial vessels and shows better tissue contrast because it is located within the subdural cerebrospinal fluid space. Therefore, localization based on the segmental level of the radicular vein on CEMRA is a more feasible strategy. Indeed, current neurosurgical treatment of SDAVF targets the initial segment of subdural venous drainage, and surgical interruption of this draining vein has become the preferred treatment for thoracolumbar SDAVFs [6,7].

On this basis, the present study proposes a radicular vein–based localization strategy for SDAVF. Using a U-Net framework with an attention mechanism, we developed a deep learning model to achieve three-dimensional segmentation of the subdural draining vein. By reconstructing the dural sac and vertebrae, the model enables panoramic three-dimensional visualization of the radicular vein, vertebral pedicle projection, and dura mater, thereby directly demonstrating the connection site between the radicular vein and the dura. This approach may allow high-precision, noninvasive, and fully automated localization of SDAVF. Considering that SDAVF is rare, real-world CEMRA data are limited and manual annotation is challenging. To meet the large-scale training requirements of deep learning, we also developed a synthetic SDAVF generation method based on spatial constraints derived from the spinal cord surface, dura mater, and intervertebral foraminal anatomy. This synthetic data generation strategy was used to create venous malformation cases for model training.

Results

model performance on train, validation, test dataset

RadicularSEUNet demonstrated rapid convergence and consistently high segmentation performance across both validation and test datasets. During training, the total loss, focal Tversky loss, and soft-clDice loss decreased sharply within the first several epochs and remained low thereafter (Fig. 1a), while the validation composite score increased from 0.727 at epoch 1 to 0.986 at epoch 20, indicating stable optimization and early performance saturation. The weighted components of the validation score, including Dice × 0.3, clDice × 0.3, and F0.5 × 0.4, showed parallel improvement, suggesting that the model achieved a favorable balance between volumetric overlap, centerline continuity, and false-positive control (Fig. 1b). In the independent validation cohort (n = 200), RadicularSEUNet achieved a median Dice of 0.986 (IQR, 0.983–0.988), median clDice of 0.987 (IQR, 0.980–0.992), median F0.5 of 0.992 (IQR, 0.991–0.994), and median composite score of 0.989 (IQR, 0.986–0.991). Comparable performance was observed in the test cohort (n = 200), with median Dice, clDice, F0.5, and composite score values of 0.986, 0.986, 0.992, and 0.988, respectively. Although a threshold of 0.5 achieved the highest validation score of 0.987, model performance remained highly stable across thresholds, with a mean of 0.986 and a standard deviation below 0.001.

Classification of spinal vascular malformations and localization of lower thoracic and lumbosacral SDAVFs

Dura-restricted AP-view MIP images allowed clear identification of radiculo-medullary and radiculo-pial arteries (Fig. 2a), thereby enabling correct differentiation of AVMs and pial AVFs (n = 8). We analyzed lower thoracic lesions (T10 and below, n = 7) together with lumbosacral lesions (n = 7) because, in these regions, the filum terminale vein (Fig. 2b, c) or radicular vein (Fig. 2d, e) is typically thick and long, which can be clearly visualized on both MIP images and RadicularSEUNet-derived vascular segmentations. In cases with long and slender radicular veins (Fig. 2f, g), RadicularSEUNet segmentation may show truncation of the radicular vein; in such cases, MIP images can provide complementary information on the continuous morphology of the radicular vein and facilitate segmental localization. For the two DSA-negative cases in our cohort (Fig. 2h, i), the final diagnosis was occult tethered spinal cord, RadicularSEUNet identified typical filum terminale vein and radicular vein patterns in both cases. Their distinction from SDAVF was based primarily on the low number of voxels (sparse vesselness) segmented by RadicularSEUNet. In patients with spinal vascular malformations, the segmented voxel numbers ranged from 8,188 to 47,088, whereas in the two negative cases, the segmented voxel numbers were 6,173 and 4,140, respectively.

RadicularSEUNet performance on upper and middle thoracic lesions

Figure 3 shows the segmentation results of 7 lesions located in the upper-to-mid thoracic spine in our cohort. At this level, the radicular veins are typically short and thin, making them particularly challenging to segment. Nevertheless, RadicularSEUNet correctly identified the radicular vein and the corresponding dural connection level in all seven cases (7/7, 100%). In contrast, the location of the radicular vein could not be determined on 2D MIP images in 3 cases (3/7, 42.9%; Fig. 3a, e, **and g**), and false-positive radicular-vein candidates were observed in several cases (yellow asterisks, Fig. 3a, c, **and f**). Venous loops adjacent to the dura mater may be misinterpreted as radicular veins on 2D images; however, these structures can be readily distinguished on 3D mask renderings. When the venous plexus shows marked lateralization and the radicular vein is extremely short (Fig. 3f), the radicular vein may appear as a small conical venous protrusion. In this setting, the conical protrusion located beneath the pedicle projection should be selected as the segmental localization landmark. In cases with very low flow and a relatively long radicular vein (Fig. 3g), the RadicularSEUNet-derived segmentation may not completely connect the radicular vein to the dura mater. Under such circumstances, the point beneath the pedicle projection should also be selected as the dural origin of the radicular vein for segmental localization.

Discussion

Using synthetic anatomical data for training, we constructed RadicularSEUNet to accurately delineate intradural radicular and bridging veins on spinal CEMRA. Combined with dura-restricted 2D MIP images, this venous anatomy-based localization approach achieved 100% accuracy in SDAVF diagnosis and

fistulous level localization in a real clinical cohort. Our results underscore that radicular vein–guided ostium localization is a feasible and effective strategy. This method can effectively reduce missed diagnoses and lower radiation exposure for both patients and clinicians, demonstrating promising clinical translational value.

SDAVF is the most common spinal vascular malformation encountered in clinical practice [8]. Its characteristic angioarchitecture consists of 4 key components: a radiculomeningeal feeder (part 1), a fistulous zone at the nerve root sleeve (part 2), an intradural radicular or bridging vein coursing beneath the pedicle (part 3), and dilated dorsal perimedullary veins (part 4) [9]. At the same time, SDAVF is also one of the spinal vascular lesions most susceptible to missed diagnosis because of its low-flow shunt physiology and subtle fistulous angioarchitecture. Both diagnosis and fistula-level localization on spinal DSA depend on successful superselective interrogation of the feeding segmental artery. In these regions, the longitudinal extent of aortic coverage is substantial, and sequential catheterization of multiple segmental arteries—particularly in older patients with a tortuous aorta—can be technically challenging, making false-negative examinations not uncommon [10] and high dose area product averaged at 395.59 Gy*cm^2 [11]. Although spinal DSA remains the reference standard, definitive diagnosis in a considerable proportion of cases is ultimately established at surgery. This likely explains the paradoxical observation in some cohorts that CEMRA may demonstrate higher diagnostic sensitivity than DSA [4,12]. Given the operator dependence of spinal DSA, CEMRA, once it achieves sufficiently high diagnostic sensitivity, may represent a realistic noninvasive alternative for both lesion detection and level localization.

In previously reported studies using MRI for SDAVF diagnosis, localization accuracy arranged from 59–88% [13–16], promising but still limited. Because of the limited spatial resolution of CEMRA, the fistulous area (part 2 of the SDAVF angioarchitecture) is generally not directly visualized. Unlike DSA, CEMRA cannot localize the fistula on the basis of the feeding segmental artery. We believe that, technically, fistula localization on CEMRA can only be achieved by identifying the intradural radicular or bridging vein (part 3). At the point where the vein traverses the dura, luminal narrowing is common and compared with the dilated dorsal veins (part 4), this venous segment is smaller and more faintly depicted on CEMRA, making image reconstruction difficult. This is likely the major factor limiting the diagnostic performance of CEMRA. In our experience, radicular veins associated with SDAVFs supplied by lower segmental arteries (T10 and below) or by branches of the internal iliac artery are relatively long and large, and the involved level can often be demonstrated on routine workstation-based threshold segmentation. Consistent with prior reports, cohorts with a higher proportion of such cases tend to show higher overall localization accuracy. The real challenge lies in the upper and mid-thoracic levels, where the radicular veins are short and thin and are therefore easily obscured by noise or eliminated by threshold-based postprocessing, resulting in localization failure. Because threshold-based segmentation is highly operator dependent, our deep learning model offers a substantial advantage over previously reported image feature–based diagnostic approaches by fully automated the segmentation task. Besides, through segmentation and reconstruction of the dural sac and spine, we achieved complete visualization

of the SDAVF angioarchitecture, thereby making the diagnosis more straightforward and anatomically intuitive.

Several diagnostic considerations should be emphasized. Firstly, the segmental level and laterality of the radicular vein do not always exactly correspond to those of the arterial feeder, although such discordance is uncommon. The radiculomeningeal artery may course along the lateral dura for one segment before connecting intradurally to the radicular vein and may connect to the contralateral intradural radicular vein through the ventral dural (Fig. 2d). In light of these patterns, when DSA targeted to the level localized by RadicularSEUNet does not reveal the fistula, angiography should be extended to the contralateral segmental artery at the same level and to the bilateral segmental arteries at the adjacent superior and inferior levels. Secondly, with a reported incidence of 1.4%, double spinal dural arteriovenous fistulas represent another special diagnostic scenario that should not be overlooked [17]. When RadicularSEUNet identifies multiple radicular veins in close proximity to the dura, particularly when the veins are separated by no more than 3 vertebral segment levels, the possibility of multiple fistulas should be carefully considered. Thirdly, it is reported that 14% SDAVF cases had a concomitant origin of the anterior or posterior spinal artery with the radicular vein [18]. Although this vascular configuration does not affect localization of the involved segment, it may complicate accurate classification of the vascular malformation subtype. Because such cases were not represented in our cohort, further validation in a larger cohort is needed to determine the accuracy of our approach in this setting.

Level localization has remained an important focus in the diagnosis and management of spinal vascular malformations, with recent progress driven by both advances in imaging modalities and improvements in postprocessing techniques. One of the most notable developments has been the introduction of photon-counting CT (PCCT). Preliminary studies have shown that PCCT improves visualization and localization of the artery of Adamkiewicz [19,20]. In addition, a two-case series reported that PCCT correctly identified an SDAVF that had been missed on DSA [21], highlighting the potential value of this low-radiation, high-resolution imaging technique for the diagnosis of spinal vascular malformations. However, PCCT only improves the clarity of the intraspinal vascular network, while visualization of the vessels passing through the intervertebral foramen remains difficult. Therefore, PCCT may still require the venous-based method proposed in this paper for localization; at present, it is still challenging to achieve localization diagnosis based on arterial flow direction like that of DSA. Another important advance has come from artificial intelligence–based postprocessing of conventional CTA images. Although several vascular segmentation foundation models have recently emerged [22,23], dedicated segmentation models specifically designed for spinal vascular malformations have not yet been well established. Zheng et al. proposed an automated AI system, SDAVFdoc, which segmented foraminal venous clusters on conventional CTA using a threshold of 42.5 as a marker for level localization [24]. This system achieved high diagnostic performance, with AUCs ranging from 0.928 to 0.954 across test sets. Compared with CEMRA-derived RadicularSEUNet, this CTA-based technique may have substantial potential for broad clinical dissemination because spinal CTA is available in most hospitals. However, from the perspective of diagnosis, intradural angioarchitecture is more familiar and clinically

interpretable than extradural venous cluster values. RadicularSEUNet provides a diagnostic representation that conforms to physicians' existing diagnostic workflow and knowledge framework. By directly visualizing the radicular vein, its dural connection, and the adjacent vertebral anatomy, RadicularSEUNet offers an intuitive and anatomically meaningful basis for SDAVF localization. Moreover, its high localization accuracy suggests the potential to reduce reliance on DSA and may ultimately contribute to a radiation-free diagnostic and therapeutic pathway for patients with SDAVF.

Although RadicularSEUNet achieved 100% accuracy for SDAVF level localization in this study, several limitations remain. First, the model requires validation in larger prospective cohorts to confirm its generalizability. Second, the spinal canal mask was used as a surrogate for the dura mater mask; future work should incorporate a dedicated dural segmentation method. Third, discontinuous segmentation occasionally occurred in long and slender radicular veins, suggesting the need for further refinement to improve venous continuity and completeness.

Methods

True CEMRA cases for model validation

From November 2024 to January 2026, we retrospectively collected 31 CEMRA cases from our spinal vascular malformation database. Cervical lesions were excluded because the diagnostic DSA procedure for these lesions was relatively easy and selective catheterization of each segmental artery was not required. Since this study focused on the localization of SDAVF (n = 21), only conditions that are easily confused with SDAVF were included: spinal arteriovenous malformation (SAVM, n = 2), pial arteriovenous fistula (n = 6), and angiography-negative cases (n = 2). Other entities, such as paraspinal fistula, spinal arteriovenous metameric syndrome, and epidural lesions, were excluded. The study adhered to the Declaration of Helsinki and was approved by the Institutional Review Board of Beijing Tiantan Hospital (approval no. KY-2026-230-01), and written informed consent was obtained from all patients.

CEMRA and DSA image acquisition

Coronal CEMRA images were acquired on a 3.0 T uMR880 scanner (United Imaging Healthcare, Shanghai, China). The acquisition parameters were as follows: matrix, 768 × 768; number of slices, 136; in-plane pixel spacing, 0.50 × 0.50 mm; slice thickness, 0.67 mm; TR, 4.46 ms; TE, 1.78 ms; flip angle, 24°; FOV, 38cm. After the acquisition of the pre-contrast mask image, an intravenous bolus injection of 15 mL of Gadopentetate Dimeglumine (Gd-DTPA) was administered at a rate of 2.5 mL/s. Fluoroscopic triggering technique was employed to initiate the dynamic contrast-enhanced scan when the contrast agent reached the aorta at the corresponding segmental level. The final images were generated by subtracting the mask image from the contrast-enhanced images.

The reference standard for the diagnosis and localization of spinal vascular malformations was 2D DSA or 3D Vaso CT. Both images were acquired on a Philips Azurion workstation (Philips Healthcare, Best,

Netherlands). After selective catheterization of the segmental artery with a 5F Cobra-2 or Simons-2 diagnostic catheter (Cordis, Miami Lakes, USA), anteroposterior 2D DSA was initially performed at a flow rate of 2 mL/s, a volume of 3 mL, and an injection pressure of 300 pounds per square inch (PSI). Once the segmental artery was confirmed to supply the vascular malformation and the catheter position was judged stable, 3D Vaso CT of the same artery was subsequently acquired. The contrast agent was diluted with normal saline at a ratio of 1:2. Acquisition parameters were as follows: flow rate, 1 mL/s; total volume, 20 mL; acquisition duration, 20 s; delay from injection start to acquisition, 3 s; voxel size, 0.27 mm isotropic. A total of 622 projections were acquired over a field of view of 22 cm or 27 cm, and the primary reconstruction matrix was 384 × 384 × 384.

Synthetic SDAVF image generation pipeline

We developed a three-dimensional synthesis pipeline to generate anatomically constrained SDAVF lesions for training RadicularSEUNet. From a pre-contrast MRI, masks of bone, intervertebral discs, and the spinal canal were segmented using TotalSpineSeg—which combines nnU-Net with an iterative algorithm for instance segmentation[25,26]. Given the lack of a direct dura output, the spinal canal mask was utilized as an anatomical proxy for the spinal dural sac. To reduce computational burden, synthesis was confined to a cropped local volume determined by the minimal bounding box containing all osseous structures, which was uniformly expanded by a 15-voxel margin (Fig. 4a). A reference SDAVF case was prepared and voxel intensities within the SDAVF were sampled to compute descriptive histogram related statistics which subsequently constrained the synthetic intensity distribution (Fig. 4b). To mimic the perimedullary compartment in which abnormal veins were allowed to course, we created a spinal cord surface shell by dilating the spinal cord mask by 2 voxels (Fig. 4c). Then, a local anatomical coordinate system was established for each case.

The spinal cord mask was converted to a physical point cloud, and principal component analysis identified the superior–inferior (SI) axis as the first principal component. Orthogonal left–right (LR) and anterior–posterior (AP) axes were derived by projecting a posterior reference vector onto the plane perpendicular to the SI axis. The cord was subsequently approximated as a smoothly varying elliptical tube: the point cloud was partitioned into SI layers, and for each layer the geometric center and 95th-percentile radii in the LR and AP directions were computed and Gaussian-smoothed to reduce local irregularities. An additional outward offset was then applied along the local surface normal so that theoretical vessel points lay slightly external to the cord before projection onto the actual shell. (Fig. 4d). Dorsal longitudinal trunks served as the primary scaffolds of the venous network. Its longitudinal extent was randomly selected as a continuous subsegment of the cord, rather than spanning the entire length. The trunk's circumferential trajectory was modeled as a dorsal-biased oscillatory function of longitudinal position. The generation stochastically selected a morphologic mode (e.g., serpentine, coiled, overcoiled) and superimposed low-frequency undulations, optional higher-frequency oscillations, and localized kinks to introduce continuous tortuosity and variable sinuosity. From this trunk, 2–5 loop branches and 0–2 hairpin branches were generated. Ventral excursions were permitted with a probability

of 0.20. All theoretical centerline points were projected onto the nearest real shell voxels using a KD-tree nearest-neighbor search, ensuring strict anatomical adherence (Fig. 4e). After the dorsal trunk had been established, secondary branches were generated from the trunk to create a more realistic malformed venous network. Two branch classes were modeled. Loop branches departed from the trunk and reconnected at a different longitudinal location, whereas hairpin branches departed and returned near their point of origin, creating a folded configuration (Fig. 4f). The trunk and all branches were assigned a radius profile along its centerline. Rasterization was performed by iterating over centerline points, defining local physical bounding boxes, and classifying voxels whose Euclidean distance to the point was less than the local radius. This process merged overlapping spherical neighborhoods into a continuous vascular solid. The dorsal trunk was allowed to be larger, with a diameter range of 1.0–3.2 mm, whereas branches were narrower, with a diameter range of 0.55–1.7 mm. Tapering and bulbous expansions were added to simulate venous pouches and stenosis. Intensity assignment occurred concurrently with voxelization. Each centerline point was assigned a base intensity sampled from reference statistics. Signal was modulated along two axes: (1) axial modulation, where intensity varied as a function of normalized arc length combined with a sinusoidal term, and (2) radial attenuation, where intensity decayed quadratically from the vessel center toward the wall to avoid unrealistically homogeneous cross-sections. Following rasterization, Gaussian blurring ($\sigma = 0.55$ mm) and mild multiplicative noise ($\sigma = 0.04$) were applied (Fig. 4g).

After generating the surface network, we created a single radicular vein to connect the lateral dura to it. Intervertebral disc masks were analyzed via connected-component labeling to extract disc centroids, which were sorted along the SI axis to define spinal segment intervals. Candidate entry zones were restricted to lie no more than 3-disc levels above the superior extent of the surface lesion, with an additional 20-mm superior offset limit. Within a 2 mm slab centered on a chosen segment, dural candidate points were evaluated in a local cross-sectional plane; the most lateral point within a lateral angular sector (± 12° jitter) was selected as the dural origin. The surface insertion point was chosen by weighting candidate vein voxels by ipsilateral preference, SI proximity to a target offset relative to the dural level (− 1.0 to + 4.5 disc levels), and Euclidean distance. The radicular centerline was then constructed as a cubic Bézier curve with four control points: the dural origin (P_0), the surface insertion point (P_3), and two intermediate points guiding the curve inward from the dura and toward the target vein. Radicular diameters ranged from 0.5–2.2 mm and underwent identical radius and intensity modulation as the surface network (Fig. 4h).

The final SDAVF mask was defined as the binary union of the surface venous network and the radicular vein. To produce the synthetic image, the cropped background volume was duplicated, original intensities within the lesion region were cleared, and the synthesized intensity maps were inserted. Outputs for each case included the synthetic image, the surface vein mask, the radicular vein mask, the combined SDAVF mask, and the cropped anatomical masks. Figure 4i shows axial, coronal, and sagittal views of a synthetic case.

Model training pipeline and network architecture

We implemented a 3D segmentation framework using a custom squeeze-and-excitation U-Net (SE-U-Net), termed RadicularSEUNet (Fig. 5). The network took a two-channel input comprising the original 3D image and the corresponding dura mask, allowing it to leverage both anatomical localization and image intensity. Prior to training, each case was cropped to the intradural space defined by the dura mask. From this region, fixed-size 3D patches of size 96×96×96 voxels were extracted. Patch sampling followed a positive-to-negative ratio of 1:3 to mitigate the extreme class imbalance inherent in vessel segmentation.

The RadicularSEUNet consisted of four downsampling and four upsampling stages. Encoder blocks used residual 3D convolutions with instance normalization, leaky ReLU activation, and a squeeze-and-excitation module to recalibrate channel-wise features. The number of feature channels increased from 16 at the first stage to 256 at the bottleneck. The decoder employed transposed convolutions for upsampling, incorporated skip connections from corresponding encoder levels, and applied residual SE blocks for feature fusion. A final 1×1×1 convolution generated a single-channel voxel-wise logit map.

Training optimized a hybrid loss that combined focal Tversky loss and soft clDice loss. The focal Tversky component emphasized difficult-to-segment vessel voxels and addressed class imbalance, while the soft clDice term promoted continuity and topological correctness in tubular structures. The model was trained using the AdamW optimizer with an initial learning rate of 2×10^-4, a weight decay of 1×10^-5, and a cosine annealing schedule. Mixed-precision training and gradient clipping were applied to improve computational efficiency and stability. Model selection was based on a composite validation score integrating Dice, clDice, and F0.5 metrics. After training, the optimal probability threshold was determined by sweeping candidate thresholds on the validation set, which was subsequently applied for inference on test synthetic cases and true CEMRA cases. All computational experiments were conducted using Pytorch on a Linux-based workstation with an NVIDIA RTX 3090 GPU (24GB memory).

Diagnosis and localization pipeline

Each CEMRA case had a confirmative DSA diagnosis pair. Within the delineated spinal dura mater, a 2D vessel image in the anteroposterior (AP) view was generated using maximum intensity projection (MIP). This dura-restricted MIP image was used to determine whether a hairpin-shaped radiculo-medullary or radiculo-pial artery supplied the vascular malformation. In the absence of such a feeding artery, the case was classified as SDAVF or a DSA-negative case and proceeded to subsequent level localization. The RadicularSEUNet segmented a 3D vessel mask within the spinal dura mater. This mask was then fused with the vertebra and dura mask to render a 3D fusion image to locate de radicular vein and its dura junction point, and a physician blinded to the DSA results determined the segmental level based on the fused image. The determined level was subsequently compared with the DSA findings to validate the ability of the model to level localization. Traditional artery-based DSA diagnosis pipeline was compared with our venous-based diagnosis pipeline in Fig. 6.

Statistics

Continuous variables were summarized as means ± standard deviations or medians with interquartile ranges, depending on whether they followed a normal distribution. A two-sided P value of less than 0.05 was considered statistically significant.

Ethics approval

The study adhered to the Declaration of Helsinki and was approved by the Ethics Committee of Beijing Tiantan Hospital, Capital Medical University (approval no. KY-2026-230-01), and written informed consent was obtained from all patients.

Data availability

The 2,000 synthetic SDAVF cases used for model training, validation and test in this study will be made publicly available upon publication of the article. Real patient data are not publicly available due to data protection restrictions but can be obtained from the corresponding author upon reasonable request.

Code availability

The training code for RadicularSEUNet will be made available on our GitHub repository.

Declarations

Competing Interests

The authors declare no competing interests.

Author Contribution

Y.P.Z designed the study, performed diagnostic DSA, wrote the code for data synthesis and model training, prepared and edited the paper. W.H.X participated in data collection and post-processing, statistics, prepared and edited the paper. X.C.W designed the CEMRA sequence, participated in MRI data acquisition, post-processing, diagnosis. L.W participated in data collection and post-processing and edited the paper. B.H participated in diagnosis, treatment of cases and edited the paper. X.D.H participated in diagnosis, treatment of cases and edited the paper. D.P.M participated in diagnosis, DSA and MRI data interpretation, treatment of cases and edited the paper. S.J.S designed the CEMRA sequence, participated in MRI data acquisition, post-processing, image interpretation and edited the paper. Y.Z.W designed the study, analyzed the data, prepared and edited the paper. W.Q.J designed the study, guaranteed the integrity of the whole study and edited the paper. All authors read and approved the final manuscript.

Acknowledgements

This work was supported by grants from and the National Key Research and Development Program of China (No. 2025YFC2511502).

Data Availability

Data availabilityThe 2,000 synthetic SDAVF cases used for model training, validation and test in this study will be made publicly available upon publication of the article. Real patient data are not publicly available due to data protection restrictions but can be obtained from the corresponding author upon reasonable request.Code availabilityThe training code for RadicularSEUNet will be made available on our GitHub repository.

References

1. Krings, T. & Geibprasert, S. Spinal dural arteriovenous fistulas. *AJNR Am J Neuroradiol* 30, 639–648 (2009). https://doi.org/10.3174/ajnr.A1485
2. Iovtchev, I. *et al.* Late diagnosis of spinal dural arteriovenous fistulas resulting in severe lower-extremity weakness: a case series. *Spine J* 15, e39-44 (2015). https://doi.org/10.1016/j.spinee.2013.08.029
3. Pang, H. *et al.* Clinical outcomes and prognostic factors in patients with spinal dural arteriovenous fistula: a nearly 10-year prospective cohort study. *J Neurosurg Spine*, 1–9 (2026). https://doi.org/10.3171/2025.12.SPINE25729
4. Saraf Lavi, E. *et al.* The Role of MRA as a Preliminary Diagnostic Tool in Diagnosing and Localizing Spinal Dural Arteriovenous Fistula. *AJNR Am J Neuroradiol* 46, 2414–2419 (2025). https://doi.org/10.3174/ajnr.A8830
5. Raymaekers, V. *et al.* Diagnostic Accuracy of 4D-MRA for the Detection and Localization of Spinal Dural Arteriovenous Fistulas: A Systematic Review and Meta-Analysis. *World Neurosurg* 193, 184–190 (2025). https://doi.org/10.1016/j.wneu.2024.10.087
6. Yang, C. *et al.* Long-term outcomes and prognostic factors in patients with treated spinal dural arteriovenous fistulas: a prospective cohort study. *BMJ Open* 12, e047390 (2022). https://doi.org/10.1136/bmjopen-2020-047390
7. Essibayi, M. A., Srinivasan, V. M., Catapano, J. S., Graffeo, C. S. & Lawton, M. T. Spinal Dorsal Intradural Arteriovenous Fistulas: Natural History, Imaging, and Management. *Neurology* 101, 524–535 (2023). https://doi.org/10.1212/WNL.0000000000207327
8. Lenck, S. *et al.* Spinal and Paraspinal Arteriovenous Lesions. *Stroke* 50, 2259–2269 (2019). https://doi.org/10.1161/STROKEAHA.118.012783
9. Kiyosue, H. *et al.* Angiographic and Clinical Characteristics of Thoracolumbar Spinal Epidural and Dural Arteriovenous Fistulas. *Stroke* 48, 3215–3222 (2017). https://doi.org/10.1161/STROKEAHA.117.019131

10. Barreras, P. *et al.* Analysis of 30 Spinal Angiograms Falsely Reported as Normal in 18 Patients with Subsequently Documented Spinal Vascular Malformations. *AJNR Am J Neuroradiol* 38, 1814–1819 (2017). https://doi.org/10.3174/ajnr.A5275
11. Ozpeynirci, Y. *et al.* Radiation Dose and Fluoroscopy Time of Diagnostic Angiography in Patients with Spinal Dural Arteriovenous Fistula. *Clin Neuroradiol* 32, 791–797 (2022). https://doi.org/10.1007/s00062-021-01130-1
12. Khalafallah, A. M. *et al.* Evaluating the diagnostic accuracy of 3D contrast-enhanced magnetic resonance angiography versus digital subtraction angiography in spinal dural arteriovenous fistulas. *Neurosurg Focus* 56, E10 (2024). https://doi.org/10.3171/2023.12.FOCUS23749
13. Wojtowicz, K. *et al.* Usefulness of time-resolved MR angiography in spinal dural arteriovenous fistula (SDAVF)-a systematic review and meta-analysis. *Neurosurg Rev* 47, 9 (2023). https://doi.org/10.1007/s10143-023-02242-7
14. Zhou, G. *et al.* Dynamic contrast-enhanced magnetic resonance angiography for the localization of spinal dural arteriovenous fistulas at 3T. *J Neuroradiol* 44, 17–23 (2017). https://doi.org/10.1016/j.neurad.2016.10.002
15. Kannath, S. K. *et al.* Utility of 3D SPACE T2-weighted volumetric sequence in the localization of spinal dural arteriovenous fistula. *J Neurosurg Spine* 25, 125–132 (2016). https://doi.org/10.3171/2015.8.SPINE141322
16. Lindenholz, A., TerBrugge, K. G., van Dijk, J. M. & Farb, R. I. The accuracy and utility of contrast-enhanced MR angiography for localization of spinal dural arteriovenous fistulas: the Toronto experience. *Eur Radiol* 24, 2885–2894 (2014). https://doi.org/10.1007/s00330-014-3307-6
17. Jablawi, F. & Mull, M. Double spinal dural arteriovenous fistulas. *J Neuroradiol* 46, 168–172 (2019). https://doi.org/10.1016/j.neurad.2018.09.004
18. Adrianto, Y. *et al.* Concomitant origin of the anterior or posterior spinal artery with the feeder of a spinal dural arteriovenous fistula (SDAVF). *J Neurointerv Surg* 9, 405–410 (2017). https://doi.org/10.1136/neurintsurg-2016-012267
19. Huang, Y. C. *et al.* Improved visualization of the Adamkiewicz artery with photon-counting CT. *Diagn Interv Imaging* (2026). https://doi.org/10.1016/j.diii.2026.01.004
20. Madhavan, A. A. *et al.* Photon Counting Detector CT Angiography for Localization of the Artery of Adamkiewicz. *AJNR Am J Neuroradiol* (2025). https://doi.org/10.3174/ajnr.A9113
21. He, N., Lyu, H., Lu, Y., Yan, F. & Jiang, H. Accurate Detection of Spinal Dural Arteriovenous Fistula With Spinal Photon-Counting Computed Tomography Angiography: A Report of Two Cases. *Stroke* 56, e44-e46 (2025). https://doi.org/10.1161/STROKEAHA.124.049475
22. Wu, J., Wen, Z., Zhou, H., Sun, N. & Zhang, Y. Geometric-topological deep transfer learning for precise vessel segmentation in 3D medical volumes. *npj Digital Medicine* (2026).
23. Wittmann, B., Wattenberg, Y., Amiranashvili, T., Shit, S. & Menze, B. in *Proceedings of the IEEE/CVF Conference on Computer Vision and Pattern Recognition.* 20874–20884.

24. Zheng, F. *et al.* Deep learning for fast screening and localization of spinal dural arteriovenous fistulas to enhance clinical workflow. *NPJ Digit Med* 9 (2026). https://doi.org/10.1038/s41746-026-02474-z
25. Warszawer, Y. *et al.* in *Proceedings on CD-ROM-International Society for Magnetic Resonance in Medicine. Scientific Meeting and Exhibition/Proceedings of the International Society for Magnetic Resonance in Medicine, Scientific Meeting and Exhibition.*
26. Isensee, F., Jaeger, P. F., Kohl, S. A., Petersen, J. & Maier-Hein, K. H. nnU-Net: a self-configuring method for deep learning-based biomedical image segmentation. *Nature methods* 18, 203–211 (2021).

Figures

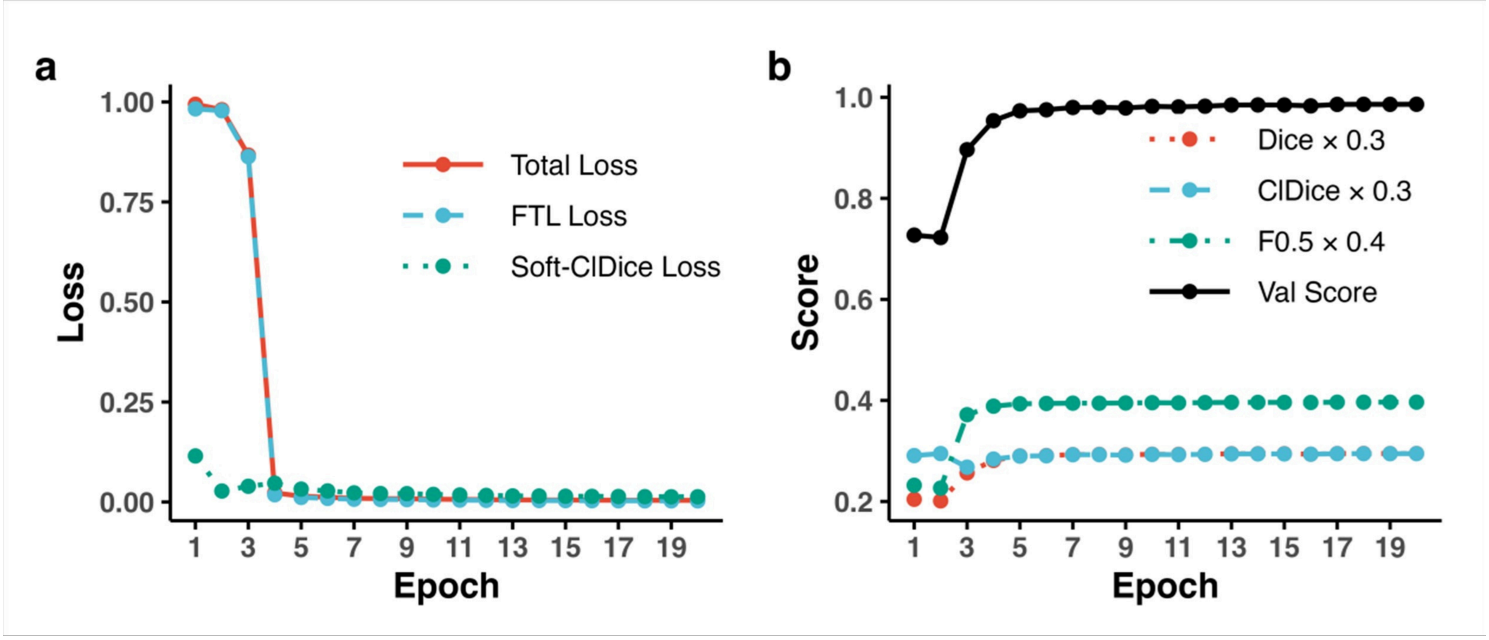


Figure 1

Training and validation metrics across epochs. **(a)** Training losses, including total loss, FTL loss, and soft centerline Dice (soft-ClDice) loss. **(b)**Weighted validation metrics (Dice coefficient × 0.3, centerline Dice × 0.3, F0.5 score × 0.4) and the combined validation score, which is the sum of the three weighted terms.

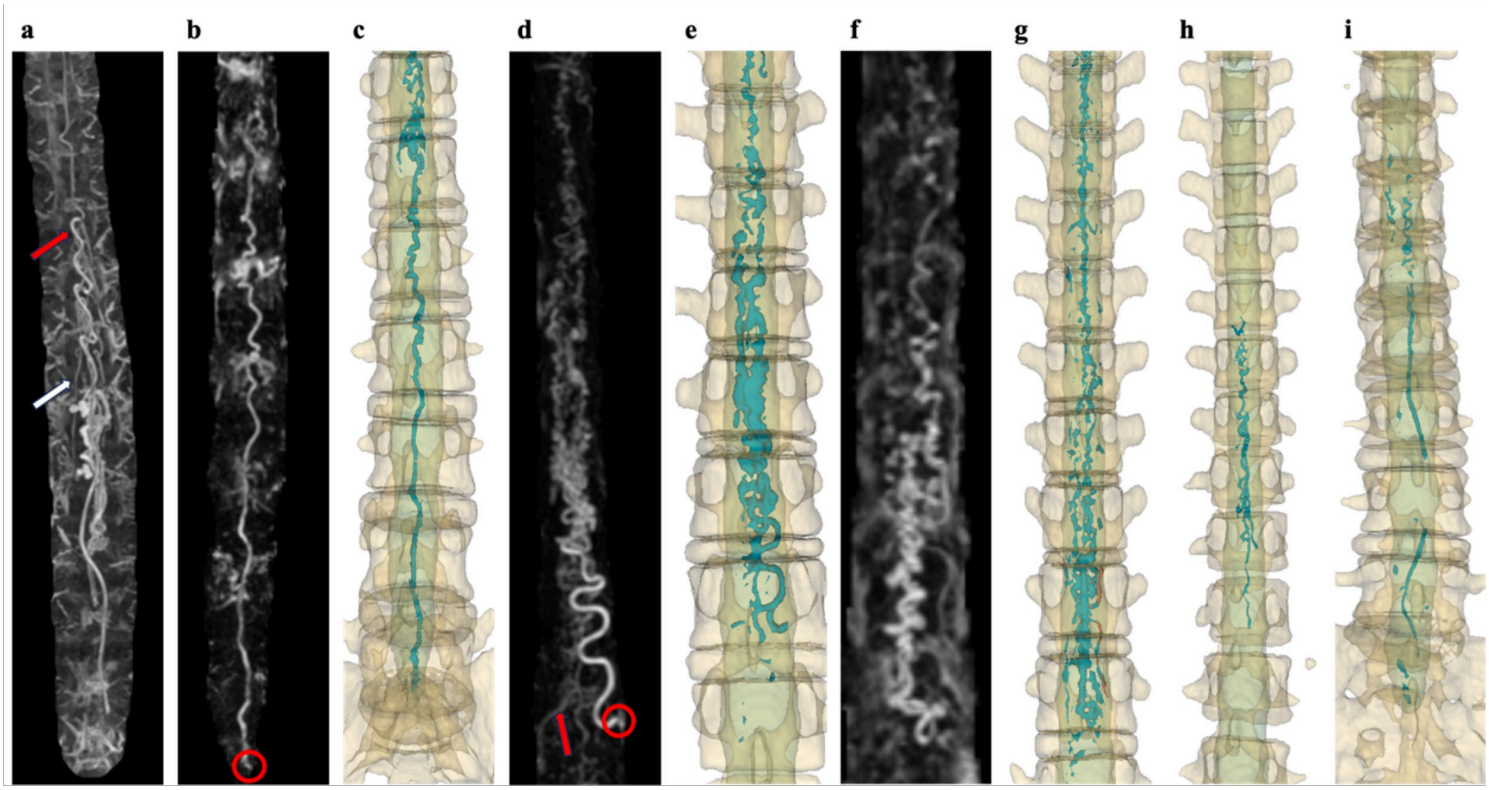


Figure 2

(a) A case of pial AVF, radiculo-medullary (red arrow) and radiculo-pial artery (white arrow) were noted. 2D dura restricted MIP image **(b)** and the model reconstructed image **(c)** of a SDAVF supplied by internal iliac artery. The red circle indicates the connection point of the filum terminale vein at the caudal end of the dural sac. **(d, e)** A left T12 SDAVF supplied by the right T12 segmental artery. Red arrows show the course of the dorsal somatic branch, through which the arterial supply reached the fistulous point on the left side of dura. The red arrowhead indicates the dural origin of the radicular vein. **(f, g)** A Left T12 segmental artery–supplied SDAVF. The radicular vein was not completely segmented along its entire course, and the missing segment is marked in red. **(h, i)** DSA negative cases with enlarged radicular vein.

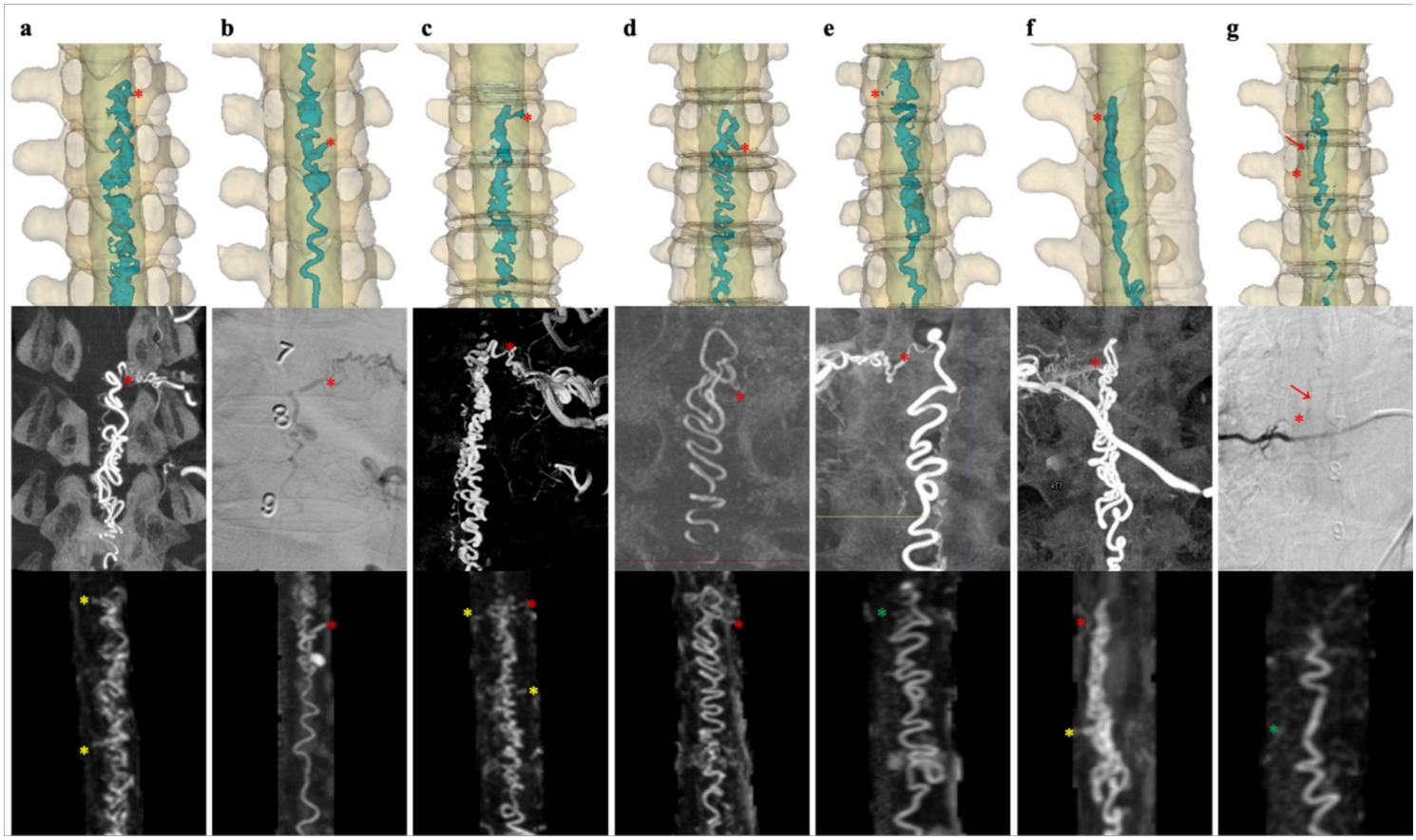


Figure 3

RadicularSEUNet performance on upper and middle thoracic lesions. Each column represents one case and contains three image sets. From top to bottom, the rows show the RadicularSEUNet-based segmentation and 3D reconstruction of the abnormal vessels, 3D vasoCT or 2D DSA images, and 2D anteroposterior-view MIP images. Red asterisks indicate the intersection between the radicular vein and the dura mater. Yellow asterisks indicate the intersection between false-positive radicular-vein predictions and the dura mater. Green asterisks indicate the dural origin of the true radicular vein that was missed on the MIP image.

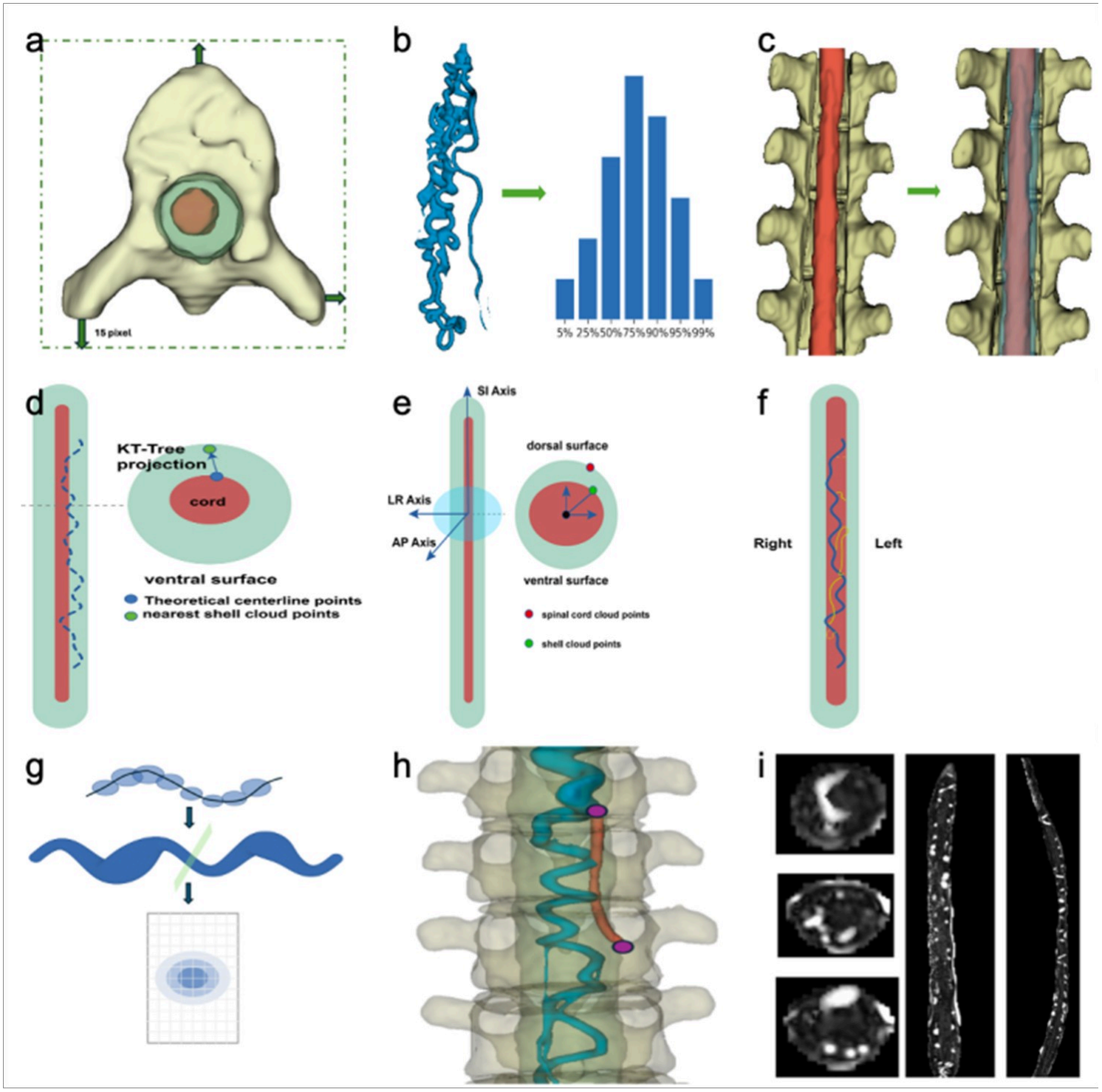


Figure 4

Synthetic SDAVF image generation pipeline. (a) Segmentation of spinal components for synthesis and volume cropping. **(b)** Reference intensity modeling. **(c)**construction of the spinal cord surface shell. **(d)** Estimation of local spinal coordinates and parametric modeling of the spinal cord surface. **(e)** Generation of dorsal longitudinal trunk. **(f)** Generation of loop and hairpin branches. **(g)**Voxelization of the surface vein network. **(h)** Disc-guided radicular vein generation. **(i)** Final fusion of SDAVF lesion with background pre-contrast image.

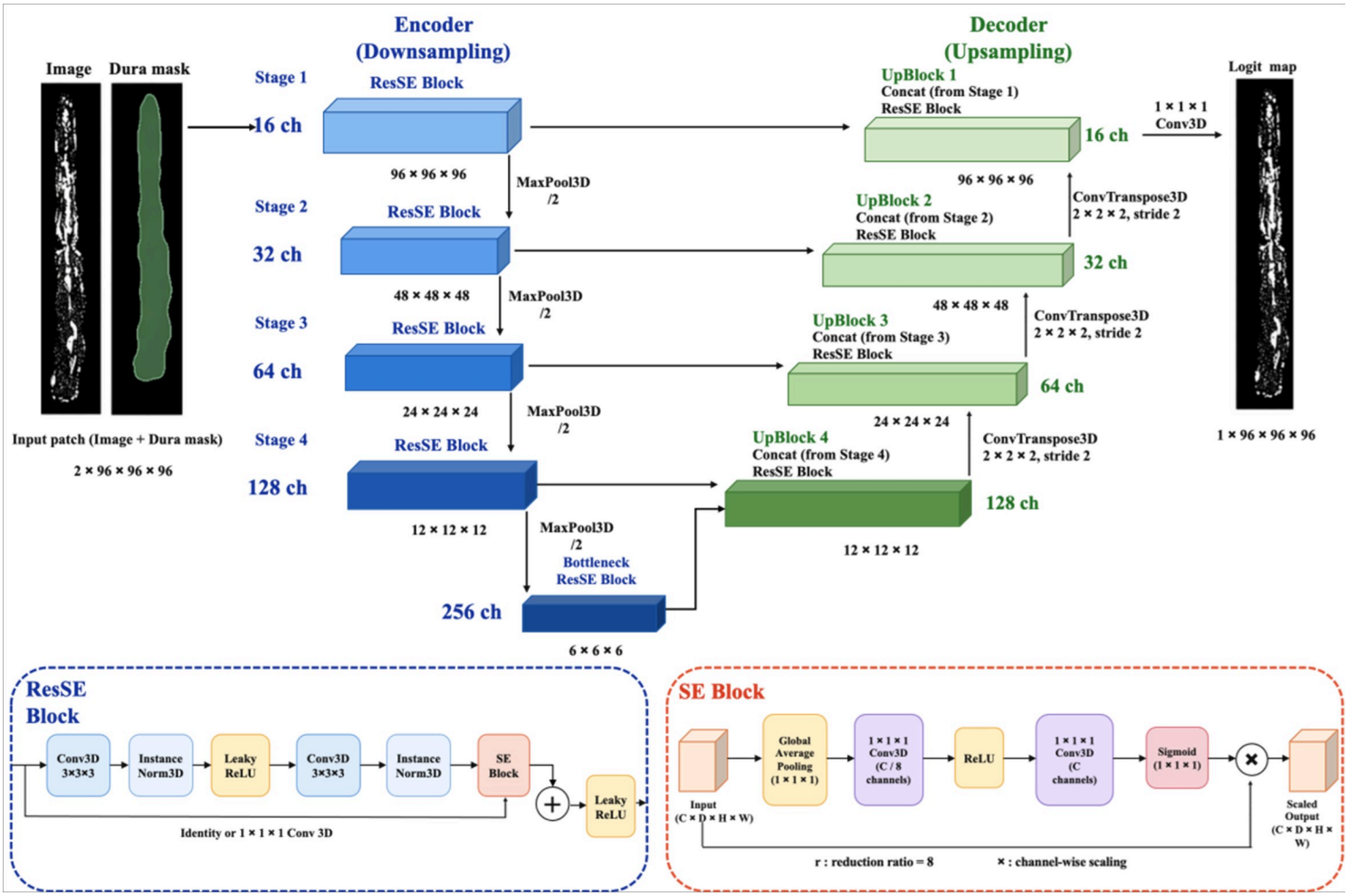


Figure 5

Model Structure of RadicularSEUNet

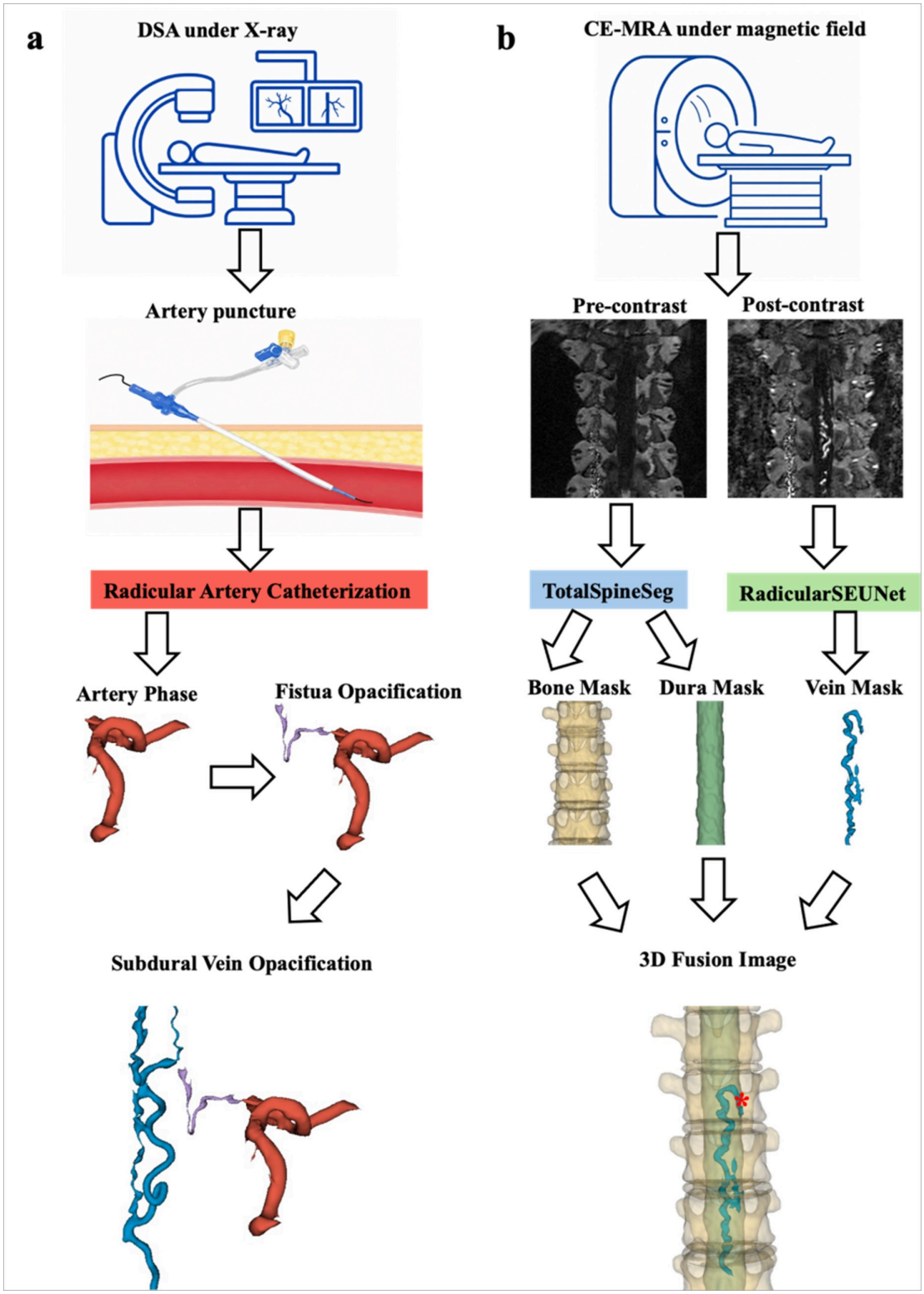


Figure 6

Artery-based (a) and venous-based level localization. (a) Traditional artery-based diagnosis is performed under X-ray guidance and requires invasive femoral artery puncture followed by selective catheterization of the radicular artery. Once the catheter is positioned, the radicular artery (red), fistulous network (purple), and subdural vein (blue) are opacified sequentially. The diagnosis of SDAVF is based on the dural location of the fistula, and the level is identified as the arterial level. **(b)** The venous-based

diagnosis begins with CEMRA acquisition. The pre-contrast image is used to segment the bone and dural mask using TotalSpineSeg, while the subdural venous mask is segmented using RadicularSEUNet. The three masks are subsequently fused into a 3D image, and the junction point (red asterisk) between the subdural vein and dura below the pedicle projection is considered the level of SDAVF.